Atmos. Chem. Phys. Discuss., 15, 22975–23004, 2015
www.atmos-chem-phys-discuss.net/15/22975/2015/
doi:10.5194/acpd-15-22975-2015

Atmospheric Chemistry and Physics Discussions

Role of radiatively forced temperature changes in enhanced semi-arid warming over East Asia

X. Guan[1], J. Huang[1], R. Guo[1], P. Lin[2], and Y. Zhang[1]

[1]Key Laboratory for Semi-Arid Climate Change of the Ministry of Education, College of Atmospheric Sciences, Lanzhou University, 730000 Lanzhou, China
[2]Program in Atmospheric and Oceanic Sciences, Princeton University, 08544 Princeton, NJ, USA

Received: 28 June 2015 – Accepted: 5 August 2015 – Published: 27 August 2015

Correspondence to: J. Huang (hjp@lzu.edu.cn)

Published by Copernicus Publications on behalf of the European Geosciences Union.

Abstract

As the climate change occurred over East Asia since 1950s, intense interest and debate have arisen concerning the contribution of human activities to the warming observed in previous decades. In this study, we investigate surface temperature change using a recently developed methodology that can successfully identify and separate the dynamically induced temperature (DIT) and radiatively forced temperature (RFT) changes in raw surface air temperature (SAT) data. For regional averages, DIT and RFT make 43.7 and 56.3 % contributions to the SAT over East Asia, respectively. The DIT changes dominate the SAT decadal variability and are mainly determined by internal climate variability, such as the North Atlantic Oscillation (NAO), Pacific Decadal Oscillation (PDO), and Atlantic Multi-decadal Oscillation (AMO). The radiatively forced SAT changes made major contribution to the global-scale warming trend and the regional-scale enhanced semi-arid warming (ESAW). Such enhanced warming is also found in radiatively forced daily maximum and minimum SAT. The long-term global-mean SAT warming trend is mainly related to radiative forcing produced by global well-mixed greenhouse gases. The regional anthropogenic radiative forcing, however, caused the enhanced warming in the semi-arid region, which may be closely associated with local human activities. Finally, the relationship between global warming hiatus and regional enhanced warming is discussed.

1 Introduction

Asia is the most sensitive area to climate change, because it comprises almost 39 % of the world's land area (White and Nackoney, 2003; Huang et al., 2013) and supports four billion people, which accounts for 66.67 % of the world population. A great portion of its drylands showed a most significantly enhanced warming in the boreal cold season over mid-to high-latitude areas (Huang et al., 2012). The non-uniform of population and economic distributed in this area led to an obvious change discrepancy

ACPD
15, 22975–23004, 2015

to the environment. Jiang and Hardee (2011) found that economic growth technological changes and population growth are the main elements in anthropogenic effects on emission, which cannot be simulated easily by numerical models (Zhou et al., 2010). More recently, there are some studies on understanding the implications of population growth, worker structure and economic intensity for various scenarios of environmental change. The anthropogenic heating resulting from energy consumption has a significant continental-scale warming effect in mid-to high-latitudes in winter based on model simulations (Zhang et al., 2013). The rapid industrialization, urbanization, population growth, and other anthropogenic activities occurred in East Asia.

In the previous studies, dynamic effects induced by greenhouse gases (GHGs) have been proposed to interpret the rapid warming over continents and non-uniformity of local warming distribution (Wallace et al., 2012). The dynamic factors exhibit their influences on surface temperature changes in terms of circulation changes, such as the North Atlantic Oscillation (NAO), Pacific Decadal Oscillation (PDO), Atlantic Multidecadal Oscillation (AMO). Guan et al. (2015) found that the dynamically induced temperature and radiatively forced temperature had opposite contributions to the surface air temperature (SAT) during the process of hiatus over the Northern Hemisphere. Most of the obvious patterns occurred over mid-to high-latitudes where they are known as places having the earliest warming (Ji et al., 2014) and a phenomenon of enhanced warming over semi-arid region (enhanced semi-arid warming, ESAW) (Huang et al., 2012). The ESAW was proposed to be caused by various factors, including changes of atmospheric circulations, sea surface temperature, interaction between land and atmosphere, feedback from snow, and so on (Hu and Gao, 1994; Zhang et al., 2001; Huang et al., 2008; Guan et al., 2009; He et al., 2014). But the roles of different factors in the process of ESAW have not been confirmed.

In this study, the roles of different factors in the process of ESAW will be investigated using a recently developed methodology that can successfully identify and separate the dynamically induced temperature (DIT) and radiatively forced temperature (RFT) changes in the raw temperature data. Section 2 introduces the datasets used in this

ACPD
15, 22975–23004, 2015

study. Section 3 provides detailed description of the dynamic-adjusted method. Section 4 shows enhanced warming in semi-arid regions and the behaviors of DIT and RFT over different regions of East Asia. It analyzes the variability of DIT and the effects of major natural factors that dominate the dynamic temperature change, and shows the change of RFT. Section 5 lists all the main findings, followed by some discussion.

2 Datasets and study area

The monthly precipitation data, land-surface air temperature data of version TS3.21, and monthly daily maximum and minimum temperature datasets are obtained from the Climate Research Unit at the University of East Anglia (Mitchell and Jones, 2005). The data cover the period of 1901–2012 with a high spatial resolution of 0.5° × 0.5°. The regionally averaged temperature trend of region k is calculated using

$$\overline{T_k} = \frac{\sum_{i=1}^{N_k} w_{ki} \times T_{ki}}{\sum_{i=1}^{N_k} w_{ki}} \quad (1)$$

where N_k is the number of grids in region k, T_{ki} is the temperature of grid i in region k, and $w_{ki} = \cos(\theta_i \times \pi/180.0)$, with θ_i is the latitude of the grid i. The temperature trend of region k is calculated by least square method based on the time series of $\overline{T}_k$.

The study area is between 30 and 50° N, and between 73 and 150° E, which almost covers the most area of East Asia. The distribution of 30 yr averaged annual precipitation from 1961–1990 (Fig. 1) illustrates most of semi-arid region (annual precipitation between 200–600 mm yr^{-1}) located in the northeast, and most of arid region is in the northwest area. It exhibits a generally increase pattern of annual precipitation from Northwest to Southeast. The wet regions are most distributed in the South area. Al-

ACPD
15, 22975–23004, 2015

though precipitation is related to surface temperature, the long-term mean precipitation is the simplest index for classifying climate regions (Huang et al., 2012).

3 Dynamical adjustment methodology

The dynamical adjustment method was first proposed by Wallace et al. (2012) and used to analyze non-uniformity of spatial warming over the Northern Hemisphere. The SAT, or the raw temperature data is divided into two parts by the dynamical adjustment method: DIT and RFT. Wallace et al. (2012) claimed the dynamical adjustment method can remove the dynamic component of the SAT induced by atmospheric circulation pattern from the raw SAT in the cold season over land areas poleward of 20° N.

The dynamical adjustment methodology used in this study (Smoliak et al., 2015) is based on the partial least square (PLS) regression of sea level pressure (SLP) to SAT. The exact process of PLS is to derive monthly dynamical adjustment of Northern Hemisphere land surface temperature field in a pointwise manner, namely, temperature time series of each grid point is a predictand. The data of temperature and SLP are standardized prior to carrying out the following dynamical adjustment steps: (1) correlate the grid-point temperature time series with its corresponding SLP to generate a one-point cross-correlation map, (2) project the monthly SLP field onto the correlation pattern, weight each grid point by the cosine of its latitude to obtain the first PLS predictor time series Z1, (3) regress this PLS predictor Z1 out of both the each grid-point temperature time series and its SLP predictor field using conventional least square fitting procedures, which can obtain a residual temperature time series and residual SLP field. Repeat these steps on the residual temperature time series and residual SLP field to obtain the respective PLS predictor Z2 and Z3, ..., Z*n*, which are mutually orthogonal. In our study, the improved dynamical adjustment methodology (Smoliak et al., 2015) has been applied to the temperature dataset and three predictors are retained, which are determined by cross-validation.

ACPD
15, 22975–23004, 2015

Following the process stated above, the components associated with changes of atmospheric circulation patterns that are expressed in terms of SLP are partitioned, and referred to as DIT variability. The rest is the residual part associated with radiatively forced factors, called the RFT. The RFT is considered as a result of build-up of GHGs, stratospheric ozone depletion, volcanic eruption, aerosol emission, local anthropogenic forcing, and so on. Therefore, we can use the dynamical adjustment method to identify the roles of DIT and RFT in the process of enhanced warming.

4 Results analysis

Figure 2 compares the variation of cold season-mean SAT of raw, dynamically and radiatively forced temperatures over East Asia in the period of 1902–2011. The curves exhibit a warming trend in the past century as a whole and an obvious warming from the 1970s to the 1990s. Then, the raw temperature change (black line) appeared a stoppage since about 2000 until now. The DIT (blue line) exhibits obvious decadal variability, with a relatively warming period from the 1970s to the 1990s and an obvious cooling period from 2000 to 2011 in the cold season. The RFT (red line) shows a rapid increasing rate since the late 1970s, which is consistent with the raw temperature data. The different evolutions of DIT and RFT indicate that the time series of DIT and RFT had different roles in the process of raw temperature variability.

Figure 3 shows the spatial distribution of raw, DIT and RFT trends over East Asia in the period of 1902–2011. Figure 3a exhibits a gradually increasing warming pattern from south to north and a strong warming trend located over northern East Asia, especially in Mongolia and Northeast China. The rate of warming was less than $0.005\,^{\circ}\mathrm{C\,year^{-1}}$ in the south of 40° N, with a small scale of cooling region over the southwest. The distribution of DIT trend (Fig. 3b) shows a basic warming background of East Asia. The warming rate over most areas was less than $0.01\,^{\circ}\mathrm{C\,year^{-1}}$, with a higher value in the northern part than in the south part as a whole, and a cooling scale was located in the Northeast of East Asia. The distribution of RFT trend (Fig. 3c)

ACPD
15, 22975–23004, 2015

exhibits a similar distribution as that of the raw temperature. It shows an obvious warming over the northern area, which reached 0.025 °C year^{-1} in some regions. A larger scale of cooling located in the southern region demonstrates that the cooling in the raw temperature was due to the radiatively factors. The difference of DIT trend distribution from RFT indicates that the influence of radiative forcing on regional temperature changes is much higher than dynamic factor.

The discrepancy of distributions between DIT and RFT trends demonstrates the roles of DIT and RFT were different. Figure 4 gives the distributions of contributions of DIT and RFT to the raw temperature in the cold season over East Asia in the period of 1902–2011. It exhibits quite different locations of high contribution for DIT and RFT. The dynamic contribution to the raw temperature (Fig. 4a) has high values over the northwest and along the coastal area of Southeast China, but the peak value is much less than its radiative value. In the spatial distribution of RFT contribution (Fig. 4b), the positive centres were located over the northeast and southwest areas, and the values were much higher than those in Fig. 4a. The difference between Fig. 4a and b illustrated the regional temperature is mainly contributed by RFT. This regional discrepancy is confirmed by the contributions of DIT (blue line) and RFT (red line) to the raw temperature as a function of annual precipitation in the cold season over East Asia (Fig. 5). Figure 5 shows that the RFT made a greater contribution than the DIT over the whole region. The contribution of RFT increased as the annual precipitation increased. Opposite to the radiative contribution, the dynamical contribution decreased with the increase of annual precipitation.

According to Huang et al. (2012), the enhanced warming occurred over the semi-arid regions. Figure 6 provides the long-term trends of DIT and RFT as a function of annual-mean precipitation. It illustrates that the RFT had a major contribution to the regional variation and showed a similar curve as the raw temperature over different regions. Both the raw data and RFT reached the peak in the area of 300–400 mm yr^{-1}. The fact that the peaks of temperature trend of both raw data and RFT occurred over semi-arid regions indicates that the radiative factors had dominated roles in the process

ACPD
15, 22975–23004, 2015

of enhanced warming over the semi-arid regions. However, the DIT trend did not show obvious difference over different areas. It kept a mean rate of 0.005 °C year^{-1}, which is far away from the 0.017 °C year^{-1} of the highest value in the drylands of the RFT trend. The greater warming rate in semi-arid region appeared in both raw temperature and RFT indicated that enhanced warming occurred in drylands is mainly leaded by RFT. It improves the previous acknowledge on the reason induced the ESAW (Huang et al., 2012), and confirms that role of radiative forced part in the process of warming over East Asia.

These results are not limited to the monthly-mean temperature; the daily minimum and maximum temperatures expressed different variability of DIT and RFT as well. Figure 7 shows the distributions of raw, dynamically induced and radiatively forced daily minimum temperature trends over East Asia in the period of 1902–2011. The raw daily minimum temperature illustrates a similar distribution as the raw monthly-mean temperature, with a stronger warming trend over northern East Asia, especially over Mongolia and Northeast China. The dynamically induced daily minimum temperature (Fig. 7b) shows a warming pattern over most areas, with a small cooling in the area along the Northeast China. The RFT trend (Fig. 7c) had an obvious warming cover the northern area, with a smaller cooling over South China than in the monthly-mean temperature.

Figure 8 is the distributions of raw, dynamically and radiatively of daily maximum temperature trends over East Asia in the period of 1902–2011. The raw daily maximum temperature trend (Fig. 8a) had a warming trend over Northern East Asia, especially over Mongolia. But the warming extent was apparently less than that in the daily minimum temperature. The cooling in the southern part was larger than that in the daily minimum temperature. The dynamically induced daily maximum temperature (Fig. 8b) shows a slight warming over most areas, with a cooling located in the area along of Northeast China. The RFT trend (Fig. 8c) had an obvious warming over the northern area, with a small cooling scale over South China, which is similar with the

ACPD
15, 22975–23004, 2015

raw daily minimum temperature. But the scale of cooling area was much larger than the radiatively forced daily minimum temperature in Fig. 7c.

In order to distinguish the regionally averaged temperature changes, the daily minimum and maximum of raw, DIT and RFT as a function of annual-mean precipitation are shown in Figs. 9 and 10, respectively. The daily minimum (Fig. 9) had a higher warming rate than the daily maximum (Fig. 10) over different regions, especially in the drylands. The peaks of RFT over the drylands in both daily minimum and maximum temperatures indicate the dominated roles of radiative effects in the regional warming. But, the DIT trend did not show a similar variability over different area in both daily minimum and maximum temperatures. The higher values of RFT of both daily minimum and maximum temperatures in the drylands emphasize the major roles of RFT in the local enhanced warming process.

The DIT as the basic background provided a relative homogenization of temperature change on a large scale. It was mainly dominated by major dynamic factors, such as the NAO (Li et al., 2013), PDO (Trenberth and Hurrell, 1994; Kosaka and Xie, 2013) and AMO (Wyatt et al., 2012; Wyatt and Curry, 2014). The correlation coefficients between DIT and NAO/PDO/AMO (Fig. 11) illustrate the influences of these dynamic factors. Figure 11a shows the distribution of the correlation coefficient between the low-frequency NAO and the DIT. It exhibits positive patterns cover most of the East Asia area, with a 95 % confidence level over Mongolia, Inner Mongolia and Northeast China; and negative patterns over India and Southwest China, with a 95 % confidence level. It suggests the strong positive influence of the NAO on the DIT over the northern area and the negative effect over the southwest of East Asia. Figure 11b is the correlation coefficient between PDO and DIT. Only the negative correlation coefficients over boundary of China and India pass the confidence level of 95 %. In South China and North China, there were positive and negative patterns, respectively. Meanwhile, the negative correlative coefficient of AMO index and DIT (Fig. 11c) covered the most area of East Asia, expect for a small positive region in the southwest of East Asia. The general spatial distribution is opposite with the distribution of the NAO.

ACPD
15, 22975–23004, 2015

The RFT variability is always considered as a result of GHGs, but more climate effects of aerosols were revealed in the recent decades (Li et al., 2011). The fast industrialization process over East Asia produced more anthropogenic GHGs and aerosols, and impacted the local climate change (Qian et al., 2009, 2011). The temperature of Coupled Model Intercomparison Project Phase 5 (CMIP5) is always marked with its correspondence to the concentration of the GHGs. In order to manifest the effects of GHGs in RFT, a comparison between RFT and a 20-model ensemble mean of CMIP5 simulations (Taylor et al., 2012) over the Northern Hemisphere is plotted (Fig. 12), which shows that the time series of the CMIP5 simulations are smoother than the observed SAT curve. But, the notable consistent exists between RFT and simulated SAT in the obvious warming period from the 1970s to the late 1990. The consistent curve of RFT and CMIP5 indicated the simulation reflect radiative part of raw temperature.

The distributions of correlation coefficients of DIT and RFT with simulated temperature of CMIP5 are expressed in Fig. 13. Figure 13a exhibits a negative pattern over most of the area expect for the boundary between Northwest China and Russia and southwest. But in Fig. 13b, the correlation coefficient of RFT with CMIP5 ensemble mean temperature has a positive pattern over most of China, which passes the 95 % confidence level, excluding the northeast of China and Mongolia. It indicates the temperature of CMIP5 has a closer relationship with RFT than DIT, namely, CMIP5 modes reflect part of raw temperatures. The high positive correlation coefficient between RFT and ensemble mean of CMIP5 confirms the dominant contribution of GHGs to the warming over a large scale. The ensemble mean temperature trend as a function of annual precipitation (Fig. 14) highlights the regional RFT over the drylands (Fig. 6). It illustrates that the enhanced warming over the semi-arid regions led by the RFT does not appear in the ensemble mean temperature, which demonstrates the CMIP5 simulations reflect temperature variability as the change of GHGs. The significant difference between RFT and simulated temperatures over the drylands indicates that the long-term global-mean SAT warming trend was mainly related to radiative forcing produced

ACPD
15, 22975–23004, 2015

by the global, well mixed GHGs. And the peak of RFT indicated the regional anthropogenic radiative forcing caused the enhanced warming in the semi-arid regions.

5 Summary and discussion

Our results confirm that the enhanced warming in the drylands was induced by the RFT. The DIT and RFT extracted from the raw temperature had different contributions in the process of temperature change. For the regionally averaged values, the DIT and RFT contributed 43.7 and 56.3 % to the SAT over East Asia, respectively. The DIT that was dominated by the NAO, PDO and AMO took a decadal variability. The RFT changes were the major contributions to the global-scale warming trend and the regional-scale enhanced warming in the semi-arid regions. Previous studies (Guan et al., 2015) pointed out the well mixed GHGs took a continuous warming effect over globe in the radiative forced temperature change. The local processes dominated the enhanced warming in the semi-arid regions. These possible local processes have been listed in Fig. 15.

The regional RFT was mainly induced by the interaction among atmosphere, land surface, snow/ice and frozen ground cover change, and regional human activities. For example, the drying of sandy or rocky soil by higher temperatures would increase surface albedo, reflecting more solar radiation back to the space. And the substantially declining of snow/ice and frozen ground change in the past 30 years, particularly from early spring through summer (Zhai and Zhou, 1997) may cause the surface temperature to increase in the cold season via the influence on albedo. The thickness of seasonally frozen ground has decreased in response to winter warming (Lemke et al., 2007), which will emit more CO_2 into the atmosphere. The net radiation in the semi-arid regions will become a radiation sink of heat relative to the surrounding regions. Besides, Multiza et al. (2010) found that local anthropogenic dust aerosols associated with human activities (Huang et al., 2015) such as agriculture and industrial activity accounted for 43 % of the total dust burden in the atmosphere. The radiatively forced

ACPD
15, 22975–23004, 2015

effect of aerosol maybe another key process in enhanced warming of semi-arid area. More investigations are needed to quantify the contribution of different local process.

Our results also well explained the co-existence of regional warming and hiatus of the Northern Hemisphere. The major interpretation of the WTS claimed that natural variability played an important role in global temperature variability (Easterling and Wehner, 2009; Wyatt et al., 2012; Wyatt and Curry, 2014; Kosaka and Xie, 2013). The RFT had a warming contribution offset the cooling effect of DIT, and result in hiatus over the Northern Hemisphere (Guan et al., 2015). According to the results of our study, the RFT had made a major contribution to global warming, where the most obvious warming appeared in the drylands. And we conclude that the long-term global-mean SAT warming trend was mainly related to the radiative forcing produced by the global, well mixed GHGs. But, the regional anthropogenic radiative forcing caused the enhanced warming in the semi-arid regions. Therefore, the hiatus as a phenomenon of global scale was not in conflict with the regionally enhanced warming in the semi-arid regions.

Acknowledgements. This work was supported by the National Science Foundation of China (41305009) and the National Basic Research Program of China (2012CB955301), and the China 111 project (No. B 13045). Fundamental Research Funds for the Central Universities (lzujbky-2015-2, lzujbky-2015-ct03).

References

Easterling, D. R. and Wehner, M. F.: Is the climate warming or cooling?, Geophys. Res. Lett., 36, L08706, doi:10.1029/2009GL037810, 2009.

Guan, X., Huang, J., Guo, N., Bi, J., and Wang, G.: Variability of soil moisture and its relationship with surface albedo and soil thermal parameters over the Loess Plateau, Adv. Atmos. Sci., 26, 692–700, 2009.

Guan, X., Huang, J., Guo, R., and Lin, P.: The role of dynamically induced variability in the recent warming trend slowdown over the Northern Hemisphere, Sci. Rep., 5, 12669, doi:10.1038/srep12669, 2015.

ACPD
15, 22975–23004, 2015

He, Y., Huang, J., and Ji, M.: Impact of land–sea thermal contrast on interdecadal variation in circulation and blocking, Clim. Dynam., 43, 3267–3279, 2014.
Hu, Y. and Gao, Y.: Some new understandings of processes at the land surface in arid area from the HEIFE, Acta Meteorol. Sin., 52, 285–296, 1994.
Huang, J., Zhang, W., Zuo, J., Bi, J., Shi, J., Wang, X., Chang, Z., Huang, Z., Yang, S., and Zhang, B.: An overview of the semi-arid climate and environment research observatory over the Loess Plateau, Adv. Atmos. Sci., 25, 906–921, 2008.
Huang, J., Guan, X., and Ji, F.: Enhanced cold-season warming in semi-arid regions, Atmos. Chem. Phys., 12, 5391–5398, doi:10.5194/acp-12-5391-2012, 2012.
Huang, J., Ji, M., Liu, Y., Zhang, L., and Gong, D.: Review of climate change research in arid and semi-arid regions, Adv. Climate Change Res., 9, 9–14, 2013 (in Chinese).
Huang, J., Liu, J., Chen, B., and Nasiri, S. L.: Detection of anthropogenic dust using CALIPSO lidar measurements, Atmos. Chem. Phys. Discuss., 15, 10163–10198, doi:10.5194/acpd-15-10163-2015, 2015.
Ji, F., Wu, Z., Huang, J., and Chassignet, E. P.: Evolution of land surface air temperature trend, Nature Clim. Change, 4, 462–466, 2014.
Jiang, L. and Hardee, K.: How do recent population trends matter to climate change?, Popul. Res. Policy Rev., 30, 287–312, 2011.
Kosaka, Y. and Xie, S. P.: Recent global-warming hiatus tied to equatorial Pacific surface cooling, Nature, 501, 403–407, 2013.
Lemke, P., Ren, J., Alley, R. B., Allison, I., Carrasco, J., Flato, G., Fujii, Y., Kaser, G., Mote, P., Thomas, R. H., and Zhang, T.: Observations: changes in snow, ice and frozen ground, in: Climate Change: The Physical Science Basis, Contribution of Working Group I to the Fourth Assessment Report of the Intergovernmental Panel on Climate Change, edited by: Solomon, S., Qin, D., Manning, M., Chen, Z., Marquis, M., Averyt, K. B., Tignor, M., and Miller, H. L., Cambridge University Press, Cambridge, UK and New York, NY, USA, 372–374, 2007.
Li, J. P., Sun, C., and Jin, F. F.: NAO implicated as a predictor of Northern Hemisphere mean temperature multidecadal variability, Geophys. Res. Lett., 40, 5497–5502, 2013.
Li, Z., Niu, F., Fan, J., Liu, Y., Rosenfeld, D., and Ding, Y.: Long-term impacts of aerosols on the vertical development of clouds and precipitation, Nat. Geosci., 4, 888–894, doi:10.1038/NGEO1313, 2011.

ACPD
15, 22975–23004, 2015

Mitchell, T. D. and Jones, P. D.: An improved method of constructing a database of monthly climate observations and associated high-resolution grids, Int. J. Climatol., 25, 693–712, 2005.
Mulitza, S., Heslop, D., Pittauerova, D., Fischer, H. W., Meyer, I., Stuut, J. B., Zabel, M., Mollenhauer, G., Collins, J. A., and Kuhnert, H.: Increase in African dust flux at the onset of commercial agriculture in the Sahel region, Nature, 466, 226–228, 2010.
Qian, Y., Gustafson Jr., W. I., Leung, L. R., and Ghan, S. J.: Effects of soot-induced snow albedo change on snowpack and hydrological cycle in western United States based on weather research and forecasting chemistry and regional climate simulations, J. Geophys. Res., 114, D03108, doi:10.1029/2008JD011039, 2009.
Qian, Y., Flanner, M. G., Leung, L. R., and Wang, W.: Sensitivity studies on the impacts of Tibetan Plateau snowpack pollution on the Asian hydrological cycle and monsoon climate, Atmos. Chem. Phys., 11, 1929–1948, doi:10.5194/acp-11-1929-2011, 2011.
Smoliak, B. V., Wallace, J. M., Lin, P., and Fu, Q.: Dynamical adjustment of the Northern Hemisphere surface air temperature field: methodology and application to observations, J. Climate, 28, 1613–1629, 2015.
Taylor, K. E., Stouffer, R. J., and Meehl, G. A.: An overview of CMIP5 and the experiment design, B. Am. Meteorol. Soc., 4, 485–498, 2012.
Trenberth, K. E. and Hurrell, J. W.: Decadal atmosphere–ocean variations in the Pacific, Clim. Dynam., 9, 303–319, 1994.
Wallace, J. M., Fu, Q., Smoliak, B. V., Lin, P., and Johanson, C. M.: Simulated versus observed patterns of warming over the extratropical Northern Hemisphere continents during the cold season, P. Natl. Acad. Sci. USA, 109, 14337–14342, 2012.
White, R. P. and Nackoney, J.: Drylands, people, and ecosystem goods and services: a web-based geospatial analysis (PDF version), World Resources Institute, available at: http://pdf.wri.org/drylands.pdf (last access: 30 January 2012), 2003.
Wyatt, M. G. and Curry, J. A.: Role for Eurasian Arctic shelf sea ice in a secularly varying hemispheric climate signal during the 20th century, Clim. Dynam., 42, 2763–2782, 2014.
Wyatt, M. G., Kravtsov, S., and Tsonis, A. A.: Atlantic multidecadal Oscillation and Northern Hemisphere's climate variability, Clim. Dynam., 38, 929–949, 2012.
Zhai, P. and Zhou, Q.: The change of Northern Hemisphere snow cover and its impact on summer rainfalls in China, Q. J. Appl. Meteorol., 8, 231–235, 1997 (in Chinese).

ACPD
15, 22975–23004, 2015

Zhang, G., Cai, M., and Hu, A.: Energy consumption and the unexplained winter warming over northern Asia and North America, Nature Clim. Change, 3, 466–470, 2013.
Zhang, Q., Wei, G., and Huang, R.: Observation and study of atmospheric drag coefficients in Dunhuang, Sci. China Ser. D, 31, 783–792, 2001 (in Chinese).
Zhou, L., Dickinson, R. E., Dai, A., and Dirmeyer, P.: Detection and attribution of anthropogenic forcing to diurnal temperature range changes from 1950 to 1999: comparing multi-model simulations with observations, Clim. Dynam., 35, 1289–1307, 2010.

ACPD
15, 22975–23004, 2015

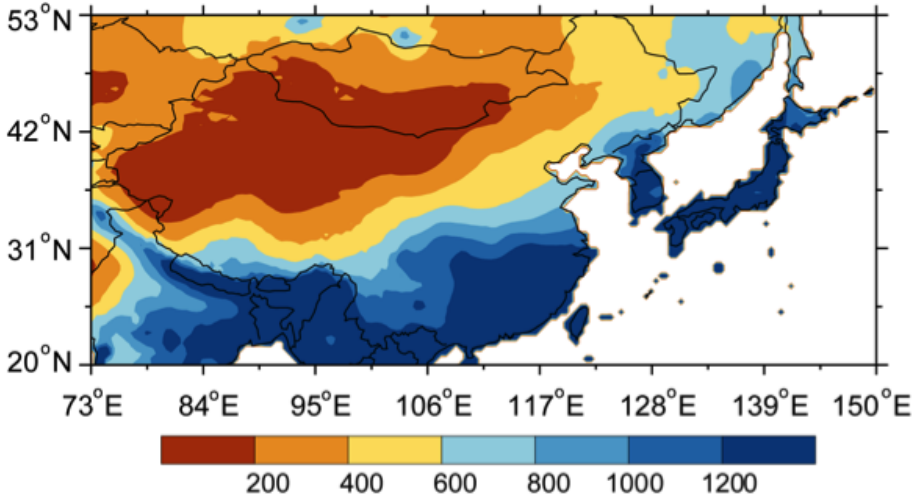

Figure 1. Spatial distribution of annual mean precipitation from 1961–1990 (mm yr^{-1}).

ACPD
15, 22975–23004, 2015

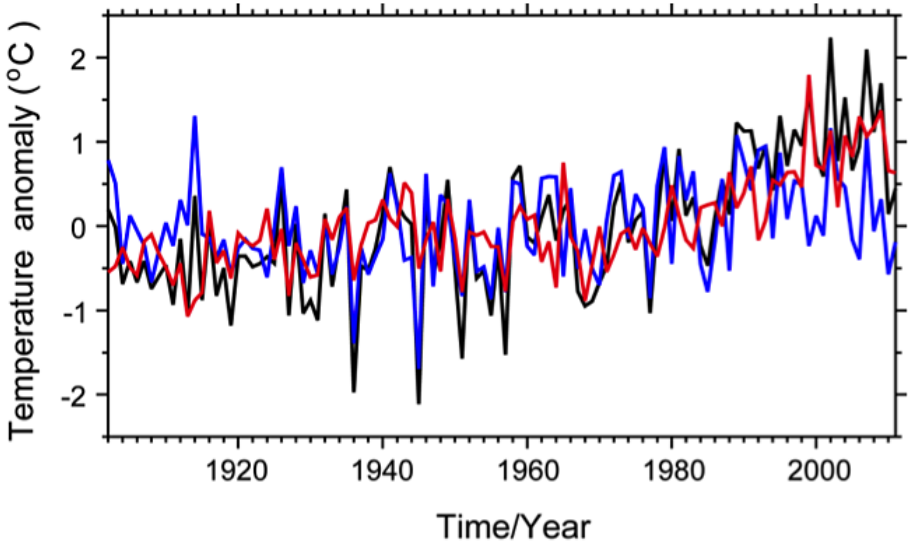

Figure 2. Time series of regionally averaged temperature anomalies of raw (black), dynamically induced (blue) and radiatively forced (red) temperatures in the cold season (November to March) from 1902 to 2011 over East Asia.

ACPD
15, 22975–23004, 2015

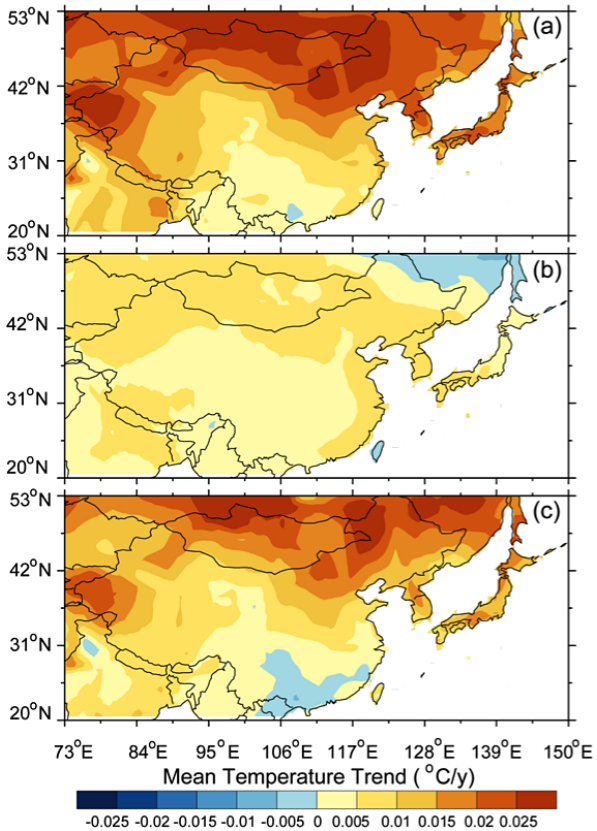

Figure 3. Spatial distribution of trend of raw **(a)**, dynamically induced **(b)** and radiatively forced **(c)** temperatures in the cold season from 1902 to 2011 over East Asia.

ACPD
15, 22975–23004, 2015

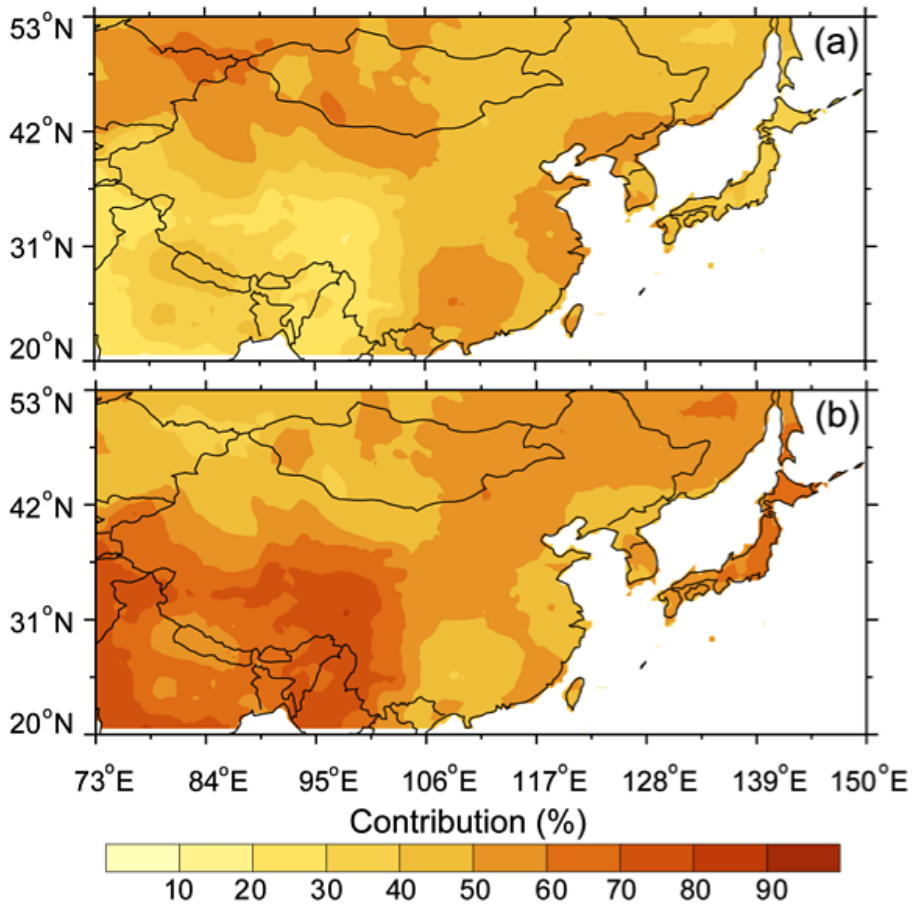

Figure 4. Spatial distribution of contribution of dynamically induced **(a)** and radiatively forced **(b)** temperatures to raw temperature in the cold season from 1902 to 2011 over East Asia.

ACPD
15, 22975–23004, 2015

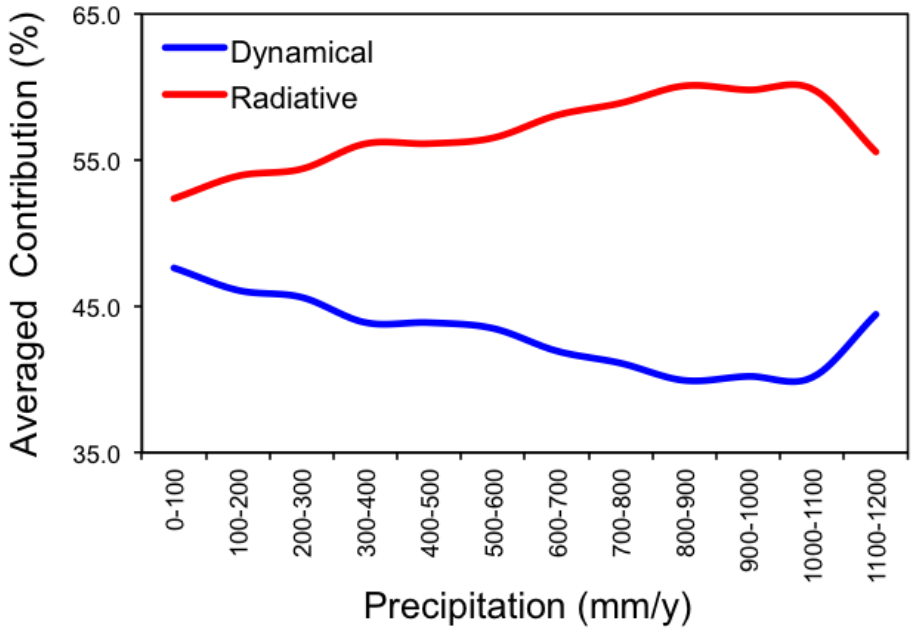

Figure 5. Contributions of dynamically induced (blue) and radiatively forced (red) temperatures to the raw temperature as a function of annual precipitation in the cold season from 1902 to 2011 over East Asia.

ACPD
15, 22975–23004, 2015

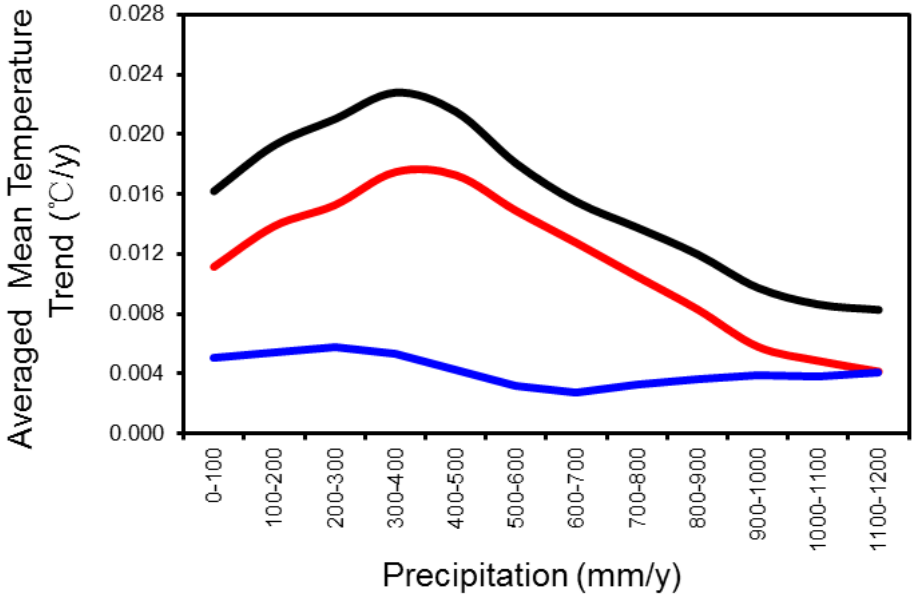

Figure 6. Regionally averaged temperature trend as a function of annual precipitation for raw (black), dynamically induced (blue) and radiatively forced (red) temperatures in the cold season from 1902 to 2011 over East Asia.

ACPD
15, 22975–23004, 2015

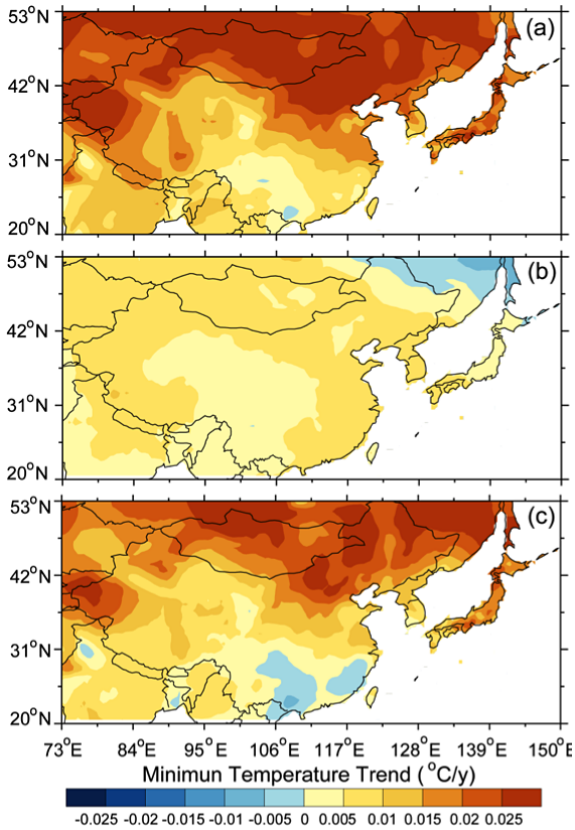

Figure 7. Same as Fig. 3, except for daily minimum temperature.

ACPD
15, 22975–23004, 2015

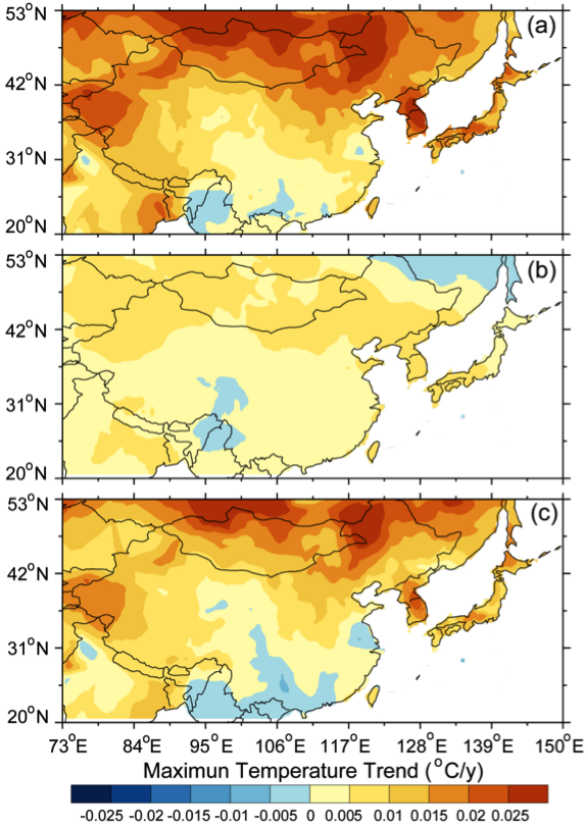

Figure 8. Same as Fig. 3, except for daily maximum temperature.

ACPD
15, 22975–23004, 2015

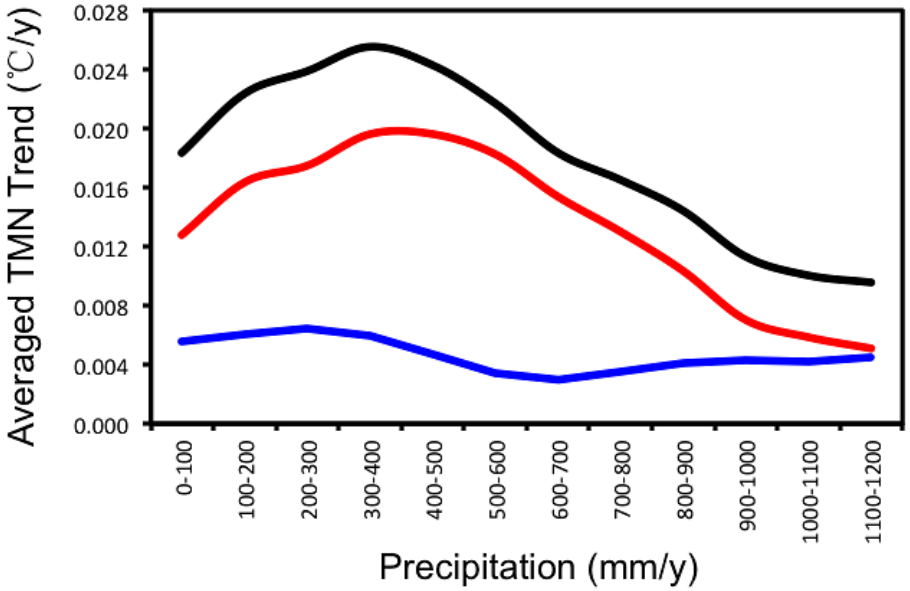

Figure 9. Same as Fig. 6, except for daily minimum temperature.

ACPD
15, 22975–23004, 2015

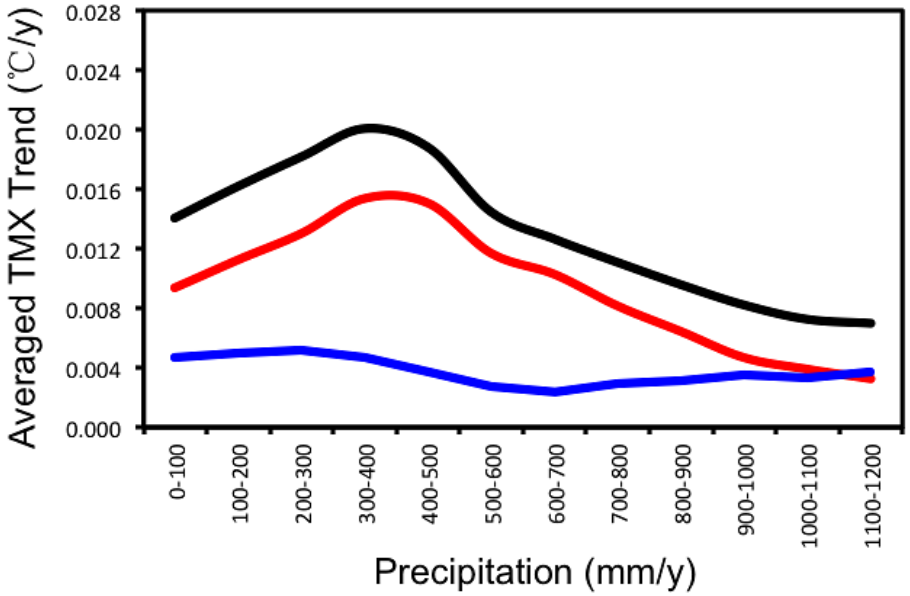

Figure 10. Same as Fig. 6, except for daily maximum temperature.

ACPD
15, 22975–23004, 2015

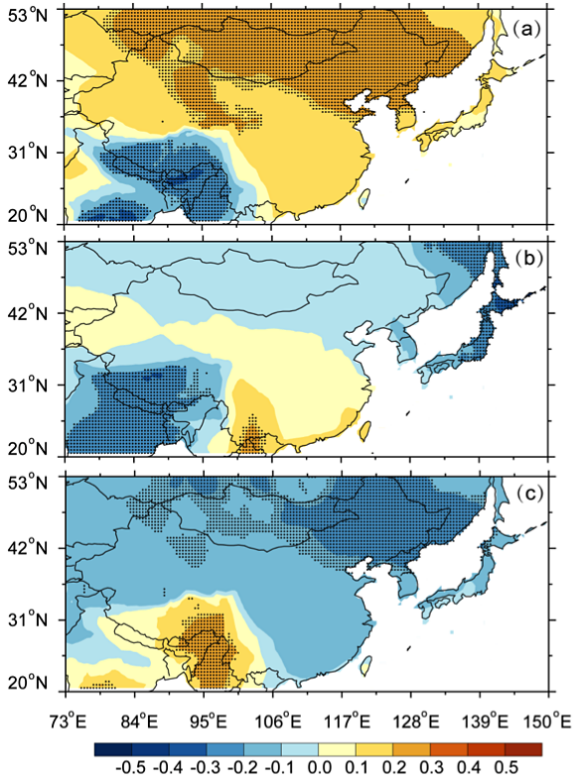

Figure 11. Spatial distribution of the correlation coefficient between detrended dynamically induced temperature and NAO (detrended and 11 year running mean) **(a)**, between detrended dynamically induced temperature and detrended PDO **(b)**, and between detrended dynamically induced temperature and detrended AMO **(c)** in the cold season from 1902 to 2011 over East Asia. The stippling indicates the 95 % confidence level according to a two-tailed Student's *t* test.

ACPD
15, 22975–23004, 2015

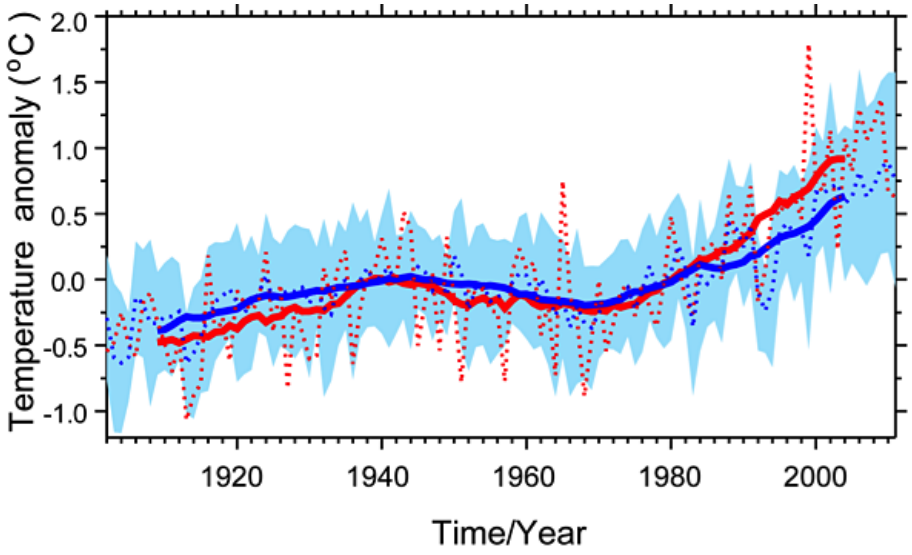

Figure 12. Time series of radiatively forced temperature (red) and ensemble-mean CMIP5 simulations (blue) based on 15 yr running mean in the cold season from 1902 to 2011 over East Asia. The blue shading indicates the standard deviation of the CMIP5-simulated field.

ACPD
15, 22975–23004, 2015

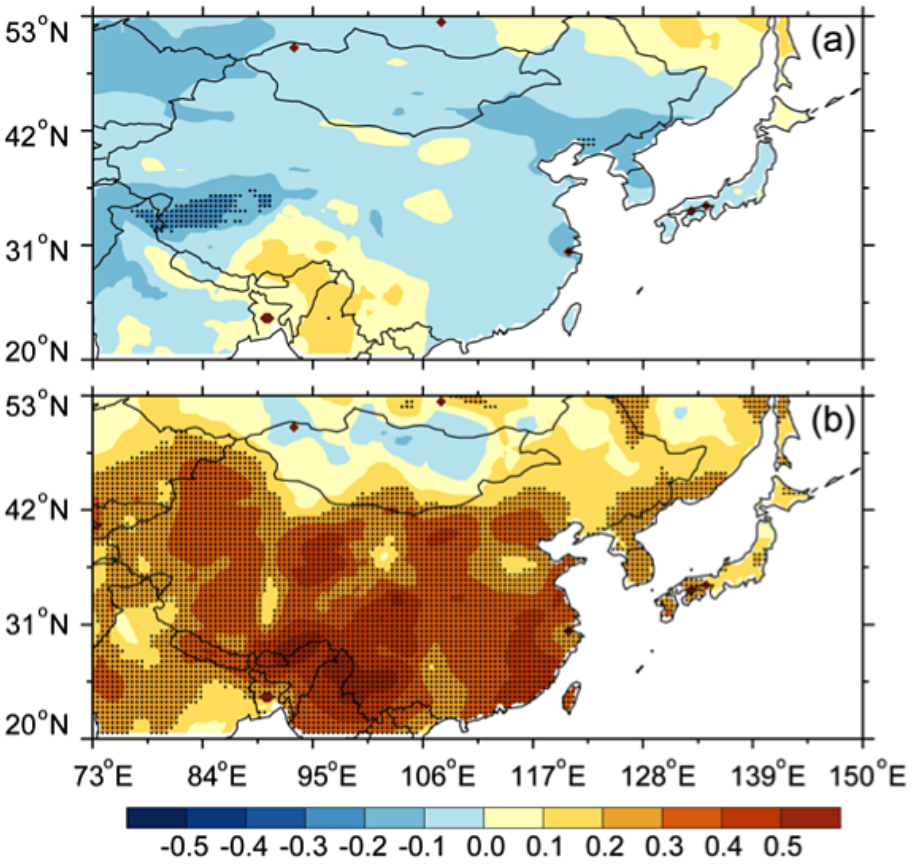

Figure 13. Spatial distribution of correlation coefficient between ensemble-mean CMIP5 simulations and dynamically induced temperature **(a)**, and between ensemble-mean CMIP5 simulations and radiatively forced temperature **(b)** in the cold season from 1902 to 2011 over East Asia.

ACPD
15, 22975–23004, 2015

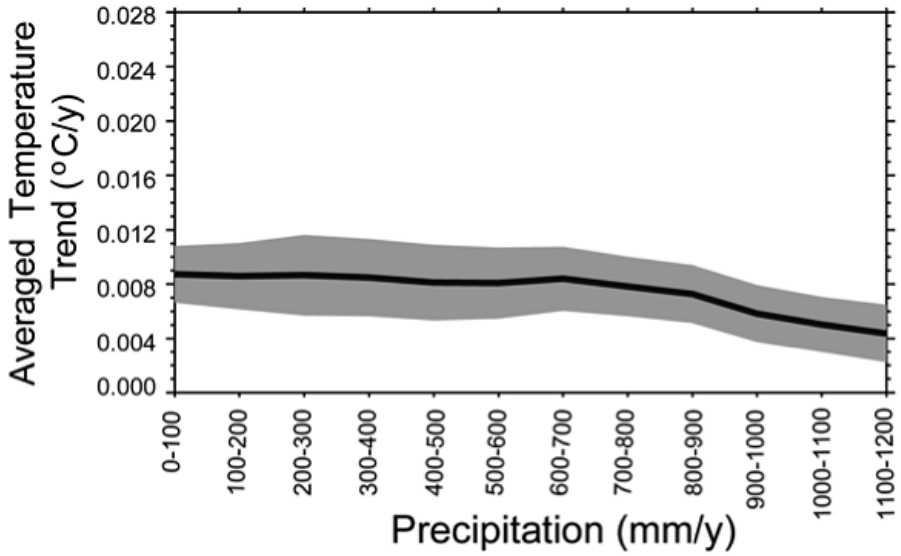

Figure 14. Regional averaged temperature trend as a function of climatological annual mean precipitation over East Asia for ensemble-mean CMIP5 simulations in cold season from 1902 to 2011, shading denotes 95 % confidence intervals.

ACPD
15, 22975–23004, 2015

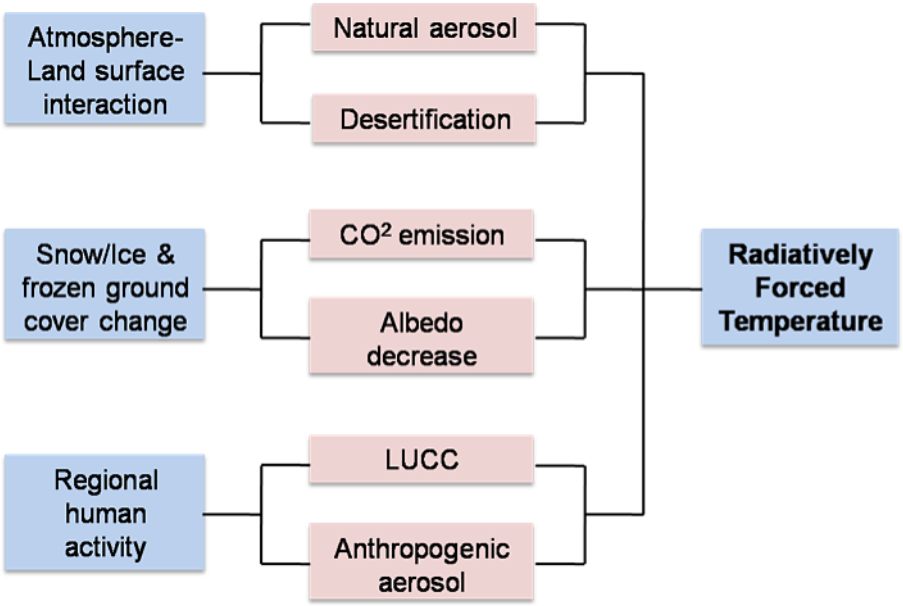

Figure 15. Schematic diagram of radiatively forced temperature.

ACPD
15, 22975–23004, 2015